Kemper, Philip ; Küstermann, Ekkehard ; Dreher, Wolfgang ; Thöming, Jorg

Experimental Investigation of Local Hydrodynamics and Chemical Reactions in Taylor Flows Using Magnetic Resonance Imaging

Book, Book chapter as: peer-reviewed accepted version (Postprint)

DOI of this document*(secondary publication): https://doi.org/10.26092/elib/3713

Publication date of this document: 20/02/2025

* for better findability or for reliable citation

Recommended Citation (primary publication/Version of Record) incl. DOI:

Kemper, P., Küstermann, E., Dreher, W., Thöming, J. (2021). Experimental Investigation of Local Hydrodynamics and Chemical Reactions in Taylor Flows Using Magnetic Resonance Imaging. In: Schlüter, M., Bothe, D., Herres-Pawlis, S., Nieken, U. (eds) Reactive Bubbly Flows. Fluid Mechanics and Its Applications, vol 128. Springer, Cham. https://doi.org/10.1007/978-3-030-72361-3_8

8. Experimental Investigation of Local Hydrodynamics and Chemical Reactions in Taylor Flows using Magnetic Resonance Imaging

Philip Kemper, Ekkehard Küstermann, Wolfgang Dreher, Jorg Thöming

Abstract In today's industrial processes reactions in dispersed gas-liquid systems are of major importance. Many products originate from gas-liquid reactions inside the bubble wake, acting as a mixing zone. High reaction yields are mainly influenced by the hydrodynamics within these zones. However, undisturbed hydrodynamic measurements of low viscous systems inside the bubble wakes are lacking. In this work we report on non-invasive MRI of gas-liquid Taylor flows. A detailed explanation of the developed MRI setup and sequence is given.

8.1 Introduction

In modern day industry gas-liquid reactions are of great importance for production processes as they serve different purposes such as oxidation, chlorination and hydrogenation. For this reason, an improvement of the selectivity and yield of these processes is aimed. Commonly, gas liquid reactions are carried out in large scale bubble columns and gas sparged tanks, which only allow efficiency measurements by globally quantifying the product stream in terms of selectivity and yield. However, these chemical reactions can only be selectively improved and optimized by investigating concentration fields and mass transfer on a local scale. Furthermore, an in-depth knowledge of the underlying flow field is required, as flow and chemical reactions are superimposed and significantly influence residence times and local concentrations. Rather than conducting experiments inside bubble swarms [1], the complexity of the investigated systems is often reduced by looking at freely rising single bubbles in large columns [2], emulating bubble swarm effects [3] or most frequently by using gas-liquid Taylor flows. They enable the investigation of single bubbles, rising inside a confined space under well-defined and reproducible measurement conditions at laboratory scale. Taylor flows are often utilized for systematic studies inside multiphase flows when looking at flow dynamics [4-8], mass transfer [9-11] and chemical reactions [12].

In confined tubes the gas phase forms the so-called Taylor bubbles, characterized by an elongated bullet shape, with a region of flow behind the bubble, referred to as the wake. Typically, Taylor bubbles fill the cross-section of the capillary, only being separated from the capillary's wall by a thin liquid film, which allows the bubble to move inside the confined space. In vertically aligned capillaries, the ratio between gravitational and surface tension forces defines whether a buoyancy driven bubble movement occurs. This ratio is also known as the dimensionless Eötvös number:

$$Eo = \frac{(\rho_{\text{liquid}} - \rho_{\text{gas}})\, g\, d_{\text{i}}^2}{\sigma} \tag{8.1}$$

It consists of the density difference between the liquid and the gas phase $(\rho_{\text{liquid}} - \rho_{\text{gas}})$, the gravitational acceleration g, the capillary diameter d_{i}^2 and the surface tension σ of the gas-liquid system [13]. Inside an air-water system, the critical number of $Eo = 4$ has to be exceeded for buoyancy driven bubble rise to occur [14]. This results in a critical capillary diameter of about d_{i} = 5.5 mm. Long-term hydrodynamic investigations are made possible by holding a buoyancy driven bubble ($Eo > 4$) in place with a countercurrent flow. The flowrate is adjusted to the terminal rise velocity of the bubble until it is spatially fixed. The terminal rise velocity of the Taylor bubble increases with larger capillary diameters, which also alters the flow inside the bubble's wake region [12, 15]. This alteration occurs due to the increasing inertia of the system at larger capillary diameters. The ratio between inertial and viscous forces is described by the dimensionless Reynolds number:

$$Re = \frac{\rho_{\text{liquid}}\, v\, d_{\text{i}}}{\eta_{\text{liquid}}} \tag{8.2}$$

The inertia depends on the fluid density ρ_{liquid}, the flow velocity v and the capillary diameter d_{i}, whereas the viscous term is only described by the dynamic viscosity of the liquid phase η_{liquid} [13]. Another dimensionless number often found in literature regarding hydrodynamics is the Capillary number:

$$Ca = \frac{\eta_{\text{liquid}}\, v_0}{\sigma} \tag{8.3}$$

It describes the interaction between interfacial forces and viscous forces. The interfacial term consists of the dynamic viscosity of the liquid phase η_{liquid} and the superficial flow velocity v_0, whereas the viscous term is only described by the surface tension σ of the gas-liquid system. Further information of transport processes is given in the book *Transport Processes at Fluidic Interfaces* [16], which resulted from the same named DFG priority programme 1506. The results helped to develop the setup of this study.

A common approach to visualize and study hydrodynamics inside Taylor flows is particle image velocimetry (PIV). Therefore, the liquid phase is seeded with fluorescent tracer particles. The particles follow the streamlines of the flow under stationary conditions. A precisely timed series of images is acquired in which local velocity vectors are determined by evaluating ensembles of tracer particles [12, 17]. The visualization of local mass transfer requires tailored reaction systems [18-20]. Some of them were recently developed within DFG priority programme 1740 to assist the experimental research. They are based on color changing reactions after contact with the gas phase. The utilized metal complexes are dissolved in water or organic solvents, acting as the liquid phase. The change in color is determined by

optical measurement techniques, meaning that they are limited to optically accessible and transparent systems.

Nuclear magnetic resonance (NMR) based imaging (MRI) is one method to face these challenges. MRI makes slice-by-slice multidimensional imaging inside opaque systems possible. It allows to directly measure positions and distances and also enables to encode different parameters, such as chemical information about the sample, diffusion coefficients and flow parameters into the complex NMR signal. The field strength dependent resonance frequency of protons builds the basis of MR imaging. The specimen is placed inside a static magnetic field with superimposed field gradients. The field gradients are essential to spatially resolve the data. An external magnetic field is applied for a short period of time in form of a radio frequency (RF) signal via a transmitter coil. A receiver coil detects the time dependent signal emitted from the system, containing spatial information of the molecules inside the sample [21, 22].

The signal intensity of an image depends on the spin density of nuclei within each examined voxel. Contrast is created by varying spin density inside the sample. Additionally, relaxation processes are used for creating image contrast: T1 (spin-lattice relaxation time), which characterizes the time needed for spin populations to return to their equilibrium state, T2 (spin-spin relaxation time), which describes the decay constant needed for the transverse magnetization to exponentially decay to zero, and T2*, (effective transverse relaxation time), which may be shorter than T2 as also the effect of spatial inhomogeneities of the static magnetic field of the signal decay are considered. As the relaxation times can change with the composition of the sample, these relaxation processes can be used to indirectly measure chemical reactions. This effect can be enhanced by utilizing paramagnetic contrast agents, leading to a strong decrease of relaxation times, particularly T1. Furthermore, chemical shift imaging can be performed to gain specific and spatially resolved information on the chemical composition of the sample, which, however, requires longer measurement times [23].

As MRI offers many possibilities, its application in the field of multiphase flows is constantly increasing [24, 25]. A review of MRI focusing on hydrodynamics is given by [26]. Experiments on 2D single phase flow velocities in simple geometries [27], as well as the quantification of bubble size distributions and bubble shapes inside gas-liquid flows [28] were successfully conducted. A first step towards the investigation of chemical reactions inside gas-liquid flows was taken by using a contrast agent inside a highly viscous gas-liquid system. It was reported on the chemical reaction around a freely and slowly rising single bubble [29]. However, all these innovative works still rely on sufficiently low flow rates, steady state conditions of the investigated flow or special chemical systems to reduce motion blurring or artifacts due to long acquisition times. This frequently leads to experimental conditions far from real application requirements. By overcoming these hurdles, real-time studies of flow dynamics inside Taylor flows can be successfully conducted under relevant conditions.

Here we report on the development of an MRI compatible Taylor flow setup for low viscous solutions. This includes the analyses of flow dynamics inside the countercurrent flow setup by PIV, the design of a custom-made radio frequency coil for signal excitation and detection, as well as the development of a MRI sequence for hydrodynamic studies inside the wake of Taylor bubbles. In a further step we demonstrate possibilities and limitations to simultaneously observe a chemical reaction taking place in the wake of a Taylor bubble.

8.2 Experimental Flow Setup for the Investigation of Taylor Flows Inside a Horizontal Bore MRI Scanner

The experimental Taylor flow setup for precise bubble generation and observation was designed in order to fulfil the spatial and material requirements of the MRI scanner. The experimental flow setup evolved during the project. This evolution is described in the following section, beginning with the first working setup for Taylor flow generation inside a horizontal bore MRI scanner.

8.2.1 Initial Version of the Flow Setup

The initial version of the flow setup is shown in Fig. 8.1. It was designed with the aim of creating a Taylor flow inside a setup of limited height, with the ability of using capillaries with different inner diameters to alter the flow dynamics inside the bubble's wake. In this approach, the fluidic connectors were horizontally aligned with the test section to minimize disturbances of the flow. A glass membrane was used at the inlet, acting as a flow straightener. Gas was injected into the setup by a thin HPLC capillary, running inside a larger HPLC capillary. The larger capillary carried the liquid phase into the test section. This particular setup allowed the use of a single HPLC connector. A gear pump with manual speed control for flow rate regulation was used to feed the liquid phase into the system. The gas phase was manually injected with a single use syringe. Outflowing liquid was collected inside a waste vessel.

Taylor bubbles were created inside round capillaries of $d_\mathrm{i} = 5$ mm, $d_\mathrm{i} = 6$ mm and $d_\mathrm{i} = 7$ mm. Additionally, rectangular capillaries with hydraulic diameters of $d_\mathrm{h} = 3$ mm, $d_\mathrm{h} = 4$ mm and $d_\mathrm{h} = 5$ mm were investigated. Taylor bubbles were created inside the rectangular capillaries, however, the liquid film between bubble and capillary ruptured in all cases within a matter of seconds, making long term measurements impossible. A treatment with piranha solution for better wettability showed no significant improvement. The de-wetting was presumably caused by the surface finish of the glass capillaries. For this reason, square capillaries were not further investigated.

The setup was successfully used for first MRI test measurements and performed well, however, two main problems were encountered. Firstly, the gear pump

induced noticeable flow fluctuations which made a spatial fixation of the bubble difficult. Secondly, the used double-capillary setup for gas and liquid supply strongly reduced the cross-sectional area passed by the fluid, resulting in high flow velocities at the inlet of the glass capillary. This led to an uncontrollable swirling motion of the fluid which further complicated the spatial fixation of the bubble. The encountered problems were addressed with an improved version of the setup.

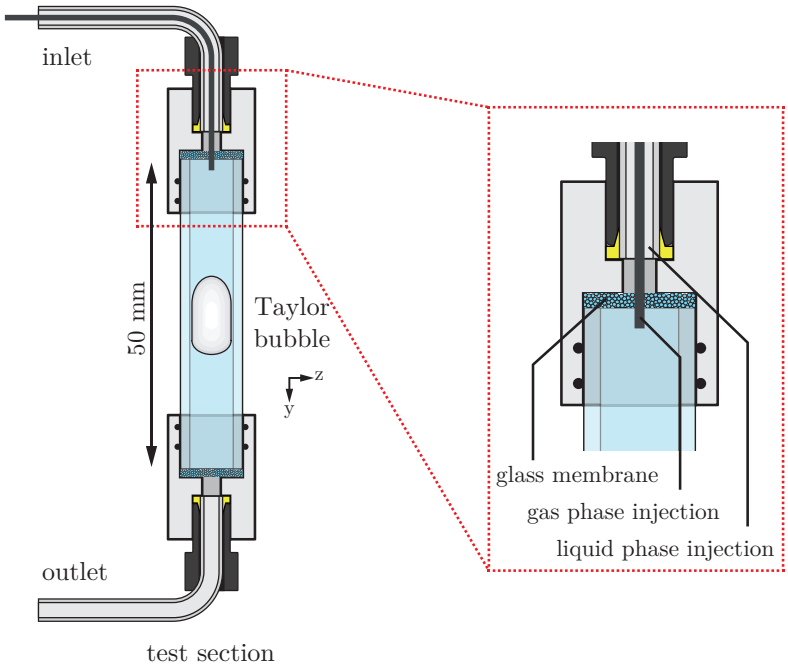

Fig. 8.1 Initial version of the flow setup, showing a glass capillary embedded into two holders. Gas is injected into the setup by a thin HPLC capillary, running inside a larger HPLC capillary used for liquid supply.

8.2.2 Improved Version of the Flow Setup

A schematic representation of the improved flow setup is shown in Fig. 8.2. The experiments were performed in a vertically aligned test section consisting of a circular borosilicate glass tube mounted into two holders. The liquid phase was fed from a pressurized vessel to prevent pump-induced fluctuations. The liquid downflow rate inside the capillary was manually adjusted by a coarse and a fine control valve. A gas-tight syringe was used to manually inject the gas phase for Taylor bubble creation. Fluid was collected in a waste vessel and the exhaust gas was

released into the fume hood. Long-term measurements were realized by keeping the buoyancy driven bubble suspended in a countercurrent flow. This presupposes a capillary diameter large enough to allow buoyancy driven bubble rise ($Eo > 4$). Rather than choosing an arbitrarily large capillary diameter, the smallest possible diameter, fulfilling the $Eo > 4$ criterion, was selected to reduce inertia (Re) inside the system. This allowed for more homogeneous flow conditions by viscous dissipation of disturbances, as the total height of the system was limited by the bore diameter of the MRI scanner and sufficiently long entrance lengths were not realizable. For this reason, a circular capillary with a diameter of $d_\mathrm{i} = 6$ mm was chosen. Additional measures were taken to further reduce disturbances of the flow. A closeup of the top holder is given in Fig. 8.2. A packed bed of glass spheres helped to deflect the lateral fluid inflow downwards into the capillary, with a fine pored glass membrane placed before the capillary, acting as an additional flow straightener. A stainless-steel tube injected the gas phase directly into the capillary.

Dimensionless numbers of this particular setup were calculated using literature data [30] for an air-water system at $T = 20$ °C to enable classification and comparability with other studies. The flow velocity was estimated by measuring the bubble's terminal rise velocity $v_\mathrm{rise} = 5.3\ mm\ s^{-1}$. The resulting dimensionless numbers are given in Table 8.1.

Table 8.1. Dimensionless numbers for an air-water system and a $d_\mathrm{i} = 6$ mm capillary

Eötvös number	Eo	4.77
Reynolds number	Re	31.69
Capillary number	Ca	$7.19 \cdot 10^{-5}$

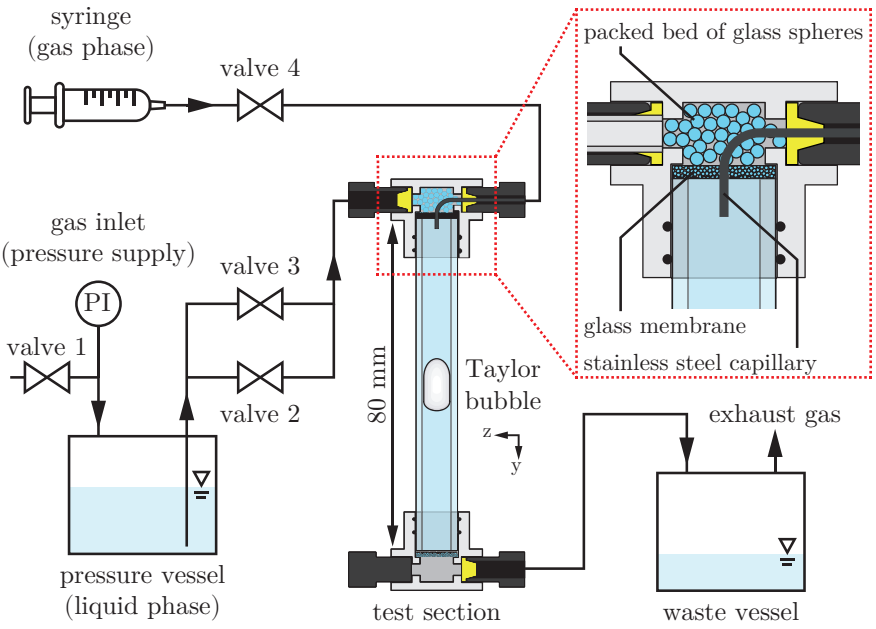

Fig. 8.2 Schematic representation of the flow setup for Taylor bubble generation. The bubble is generated and spatially fixed inside the test section by a countercurrent flow. A close-up of the test section's inlet reveals the internal components for flow straightening and bubble generation.

8.2.3 Hydrodynamic Investigation by PIV

To get an overall understanding of the prevailing flow dynamics inside the setup, the local hydrodynamics inside the test section and around the Taylor bubble were investigated with particle image velocimetry (PIV). For this purpose, fluorescent particles were excited using a laser and particle movement was recorded with a highspeed camera. Fluorescence excitation was performed with a 12 W ($\lambda =$ 447 nm) continuous wave laser (CNI laser, China) combined with a laser sheet optic to achieve an almost 2D illumination plane inside the test section. The light sheet was aligned along the capillary's center plane. Highspeed image acquisition was performed with a pco.dimax HS4 (PCO AG, Germany) CMOS camera at a frame rate of 300 Hz and an exposure time of 900 µs. A 105 mm 1:2:8 DG macro lens (Sigma, Japan) allowed a high magnification and a shallow depth of field (DOF). A spatial resolution of 0.012 mm x 0.012 mm was achieved. The DOF was estimated [31] to be 0.725 mm with the given optical setup. A high-pass filter ($\lambda = 475$ nm, Carl Zeiss, Germany), mounted in front of the lens, shielded the camera's CMOS chip from scattered laser light. The camera was focused on the center plane of the capillary. Refractive index matching (RIM) minimized optical disturbances at the curved capillary interface. For this purpose, a borosilicate box was built around the

test section. The box contained a glycerol/water mixture [32], matching the refractive index of the borosilicate glass ($\eta = 1.473$). A fluorescent polystyrene particle solution (Polyscience Fluoresbrite Carboxy YG Microspheres 4.5 µm, packed as 2.5 % aqueous solution, $\lambda_{ex} = 441$ nm, $\lambda_{em} = 486$ nm) was suspended ($1\ \mathrm{ml\,l^{-1}}$) in ultrapure water and used as the liquid phase. Bubbles were manually created using air. Mass transfer and bubble shrinkage was avoided by saturating the ultrapure water with air. The investigated Taylor bubbles had a length to diameter (l/d) ratio between 2 and 3.

PIV images were captured at the capillary's center plane. The camera was focused to the phase boundary of the rear cap with a high precision linear stage. A bubble was introduced, manually placed and held within the experimental reference frame. A series of 3000 to 4000 images was captured at a frame rate of 300 Hz and saved. The images were postprocessed in MATLAB before applying the actual PIV algorithm. They were cut to size and background noise was removed by using a threshold. The particle intensity was at least two times higher than the background signal. A 2d cross-correlation approach (xcorr2) with a manually chosen ROI was used to align the phase boundary layer at the bubble's rear cap on all images. The bubble position of the first image acted as reference. A movement of $\pm\ 100$ pixel around the reference position was tolerated. 1200 valid and consecutive images were manually checked for outliners and saved for the PIV analyses.

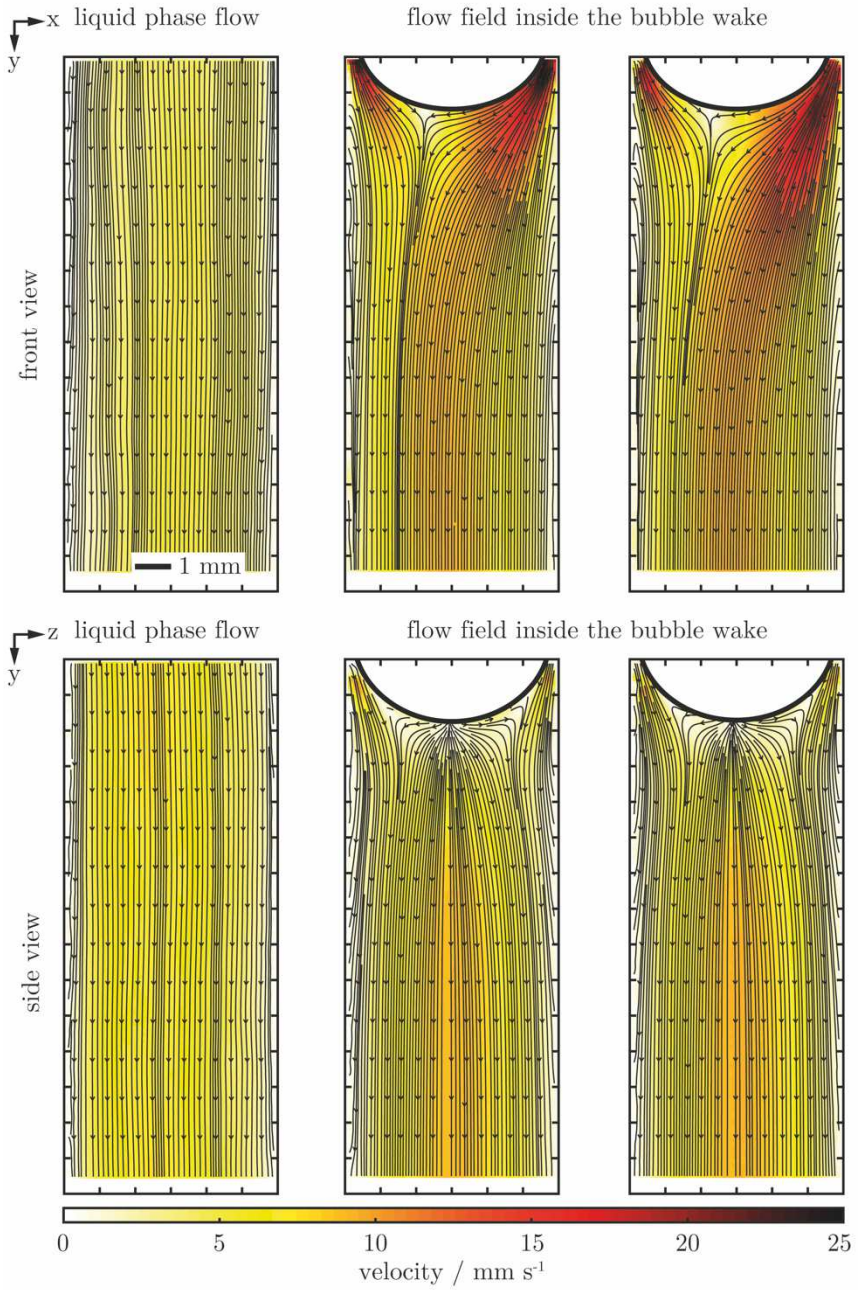

Fig. 8.3 Results of the hydrodynamic PIV analyses inside two cross sections (Y-X, Y-Z). The downflow inside the empty test section, as well as the flows inside the wake region of independent bubbles are shown. The 2D in-plane flow direction of the 3D flow field is represented by streamlines. The velocity magnitude is color coded and the gas liquid interface of the bubble is indicated.

The flow field was analyzed by an ensemble correlation algorithm in MATLAB using the PIVlab 2.31 toolbox [33]. Interrogation window sizes were successively decreased from 64 x 64, over 32 x 32 to 16 x 16 pixel. The overlap was set to 50 %.

The hydrodynamic results of the ensemble PIV analyses inside two cross sections (Y-X, Y-Z) are shown in Fig. 8.3. The full 2D flow field inside the measurement plane is represented by streamlines. The velocity magnitude is indicated by color coding. Each view shows the liquid downflow inside an empty test section, followed by the flow field inside the wake region of two independent bubbles, held in a countercurrent flow. The streamlines of the fluid inside the empty test section show a rather homogeneous flow along the capillary. Only minor disturbances in radial direction are noticeable. However, looking at the wake region of a spatially fixed bubble, the flow patterns inside both cross sections differ significantly. Inside the Y-X plane very pronounced and unequal flow velocities on the left and right side of the bubble's cap are present, with streamlines pointing towards the capillary's center line. In contrast, the Y-Z plane shows velocities up to one order of magnitude lower and the streamlines are pointing away from the capillary's center line. Furthermore, an additional flow arises in the vicinity of the bubble. This is explained by out of plane motion of the 3D flow field. The investigation of a series of independent bubbles has shown a reproducible asymmetrical behavior of the flow field without vortices or back mixing. This enables the use of PIV as a reference method for the MRI results inside the given setup.

8.3 Development of an MRI Setup for Taylor Flow Investigations Inside a Horizontal Bore MRI Scanner

MRI experiments were performed inside a BioSpec 70/20 USR (Bruker Biospin MRI GmbH, Germany) 7 T MRI scanner with a magnetic field gradient insert BGA 12S2 ($d_\mathrm{i} = 116$ mm, maximum gradient strength $= 441$ mT m^{-1}). A custom-made radio frequency coil was built around the test section for excitation and reception of the magnetic resonance signal. The design of the RF coil is based on the principle of a loop-gap resonator, which was connected to a preamplifier of the MRI hardware by an inductively coupled single turn pickup coil [34]. Similar to the flow setup, the design of the RF coil and the MRI setup is described in the following section.

A first prototype of a loop-gap resonator was constructed around a single-use syringe as a proof-of-principle, investigating how it performs at the required size. Results of the first MRI measurements are shown in Fig. 8.4. A 5 ml single-use syringe filled with deionized water acted as a specimen and was placed inside the coil. The signal of the liquid phase was mapped in 2D and 3D using a FLASH sequence, resulting in a strong and rather homogeneous signal. The first provisionally built version of the loop-gap resonator performed well, with promising results in mapping the water phase and was therefore further developed.

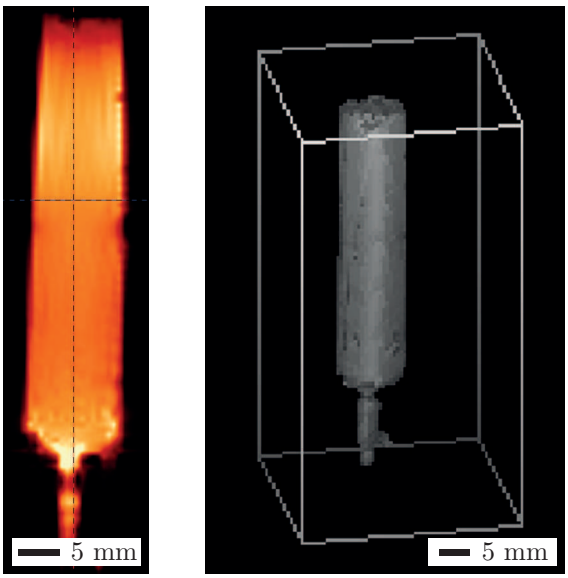

Fig. 8.4 Result of the first MRI measurement using a prototype of the loop-gap resonator. A 5 ml single-use syringe filled with deionized water acted as a specimen. The signal of the liquid phase was mapped in 2D and 3D using a FLASH sequence. The 2D image represents a single slice from the 3D volumetric data.

The improved loop-gap resonator was built around an acrylic tube as shown in Fig. 8.5a. A resonant circuit is formed by the inductance of the copper foil, glued onto the acrylic tube, and the capacitance of the chip capacitors, soldered onto the copper foil. A variable tuning capacitor allowed manual frequency matching to the ^{1}H NMR frequency at 7 T of approximately 300.3 MHz. The correct distance between the coupled coils is of crucial importance as it alters the impedance of the system. Matching it to 50 Ω avoids reflection losses and allows even small signals to be detected [35]. The vertical position of the pickup coil could be precisely adjusted by a 3D printed scissor-lift mechanism as depicted in Fig. 8.5b. A special holder was designed, enabling exact positioning of the test section inside the center of the MRI scanner. The holder was machined from PTFE (Polytetrafluoroethylene) which is proton-free and does not interfere with the ^{1}H NMR signal. A modular design allowed for safe and rigid mounting of the used components. An early CAD design of the holder with added parts is shown in Fig. 8.5c. The CAD construction of the setup helped to make full use of the limited size inside the MRI scanner. Fig. 8.5d shows a photograph the latest MRI setup using the improved flow setup.

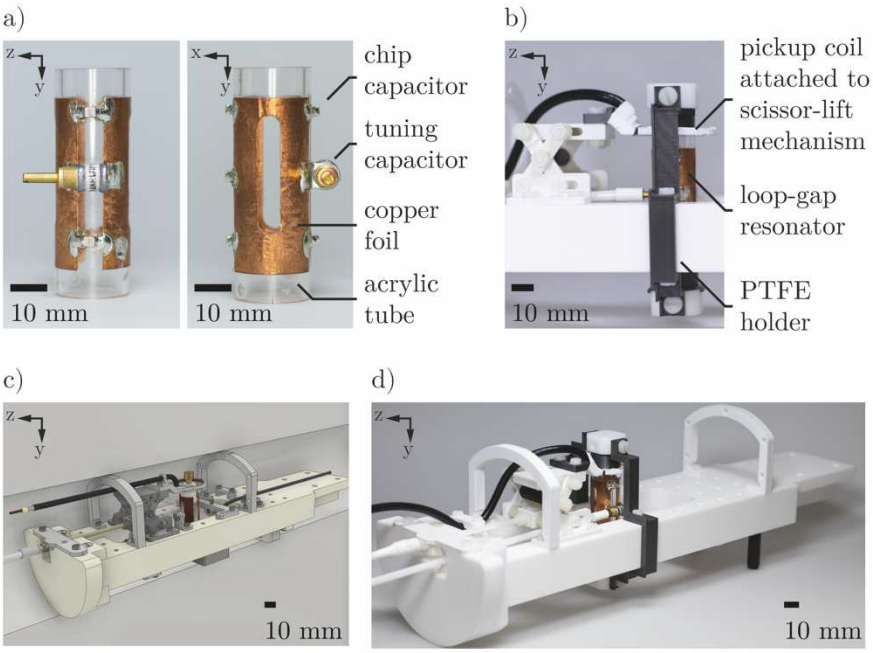

Fig. 8.5 Parts of the experimental MRI setup. a) The loop-gap resonator consists of a copper foil, glued onto an acrylic tube. Chip capacitors and a tuning capacitor are soldered to the copper foil, forming the resonant circuit. b) The pickup coil is attached to the height adjustable scissor-lift mechanism for impedance matching. c) All parts are designed and fitted using CAD. d) The components are mounted to the PTFE holder, which is inserted into the MRI scanner.

In-process monitoring of the test section was enabled with a camera (Grasshopper FLIR Systems Inc, United States) connected to an optical fiber endoscope (Hinze Optoengineering GmbH, Germany). This allowed a precise bubble adjustment during flow experiments inside the test section while being inserted inside the MRI scanner.

Further tests were performed with the improved loop-gap resonator. The signal intensity of a capillary filled with deionized water was measured using an MRI FLASH sequence. An overlay of the acquired MRI data and a CAD model of the specimen is shown in Fig. 8.6. The measured signal intensity of the water is color coded. The overlay clearly shows a good dimensional accuracy of the data, as no scaling was applied. The signal intensity fluctuates slightly within the center region of the capillary and clearly decreases at the bottom holder. This is mainly caused by a strong signal loss towards the ends of the loop-gap resonator and may also depend on the material of the capillary holder, meaning that further flow experiments should be conducted around the center of the resonator.

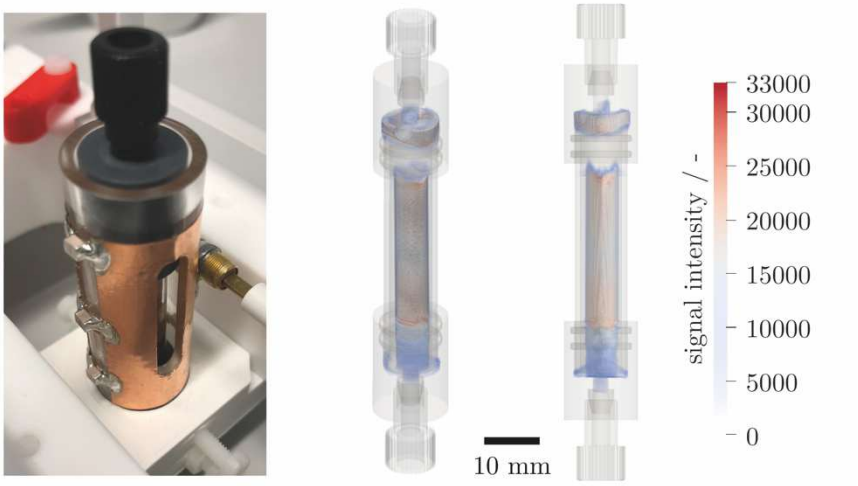

Fig. 8.6 A capillary filled with deionized water is placed inside the loop-gap resonator. The acquired MRI data and the CAD model of the specimen are overlaid to check for dimensional accuracy of the data. The signal intensity is color coded.

An attempt has been made to extend the measurement range by using a longer loop-gap resonator, covering the complete test section of the improved flow setup. To this end, a second resonator was calculated and built. A capillary filled with deionized water was used for signal intensity measurements. A comparison of both, the short and the long resonator, is given in Fig. 8.7. The signal intensity of two cross-sections (Y-X, Y-Z) along the capillary's center line is shown. The short resonator shows a rather constant signal intensity with only minor fluctuations inside both views. The signal loss towards the ends of the loop-gap resonator is clearly visible, as previously seen in Fig. 8.6.

The long resonator was constructed to extend the field of view by 30 mm in axial direction. Unfortunately, this extension comes at a cost: The Y-Z plane shows an unevenly distributed signal intensity which is strongly pronounced at the center and towards the ends of the resonator. In between, a significant loss of signal is observed. The Y-X plane reveals a region of high intensity at the right side of the resonator. The position of greater intensity corresponds to the placement of the variable tuning capacitor. Several rearrangements of the capacitors have not improved the inhomogeneous intensity inside the longer resonator. The exact cause was not further examined, but the effect can be caused by eddy currents. Due to the inhomogeneous intensity distribution, the longer loop-gap resonator was not considered further.

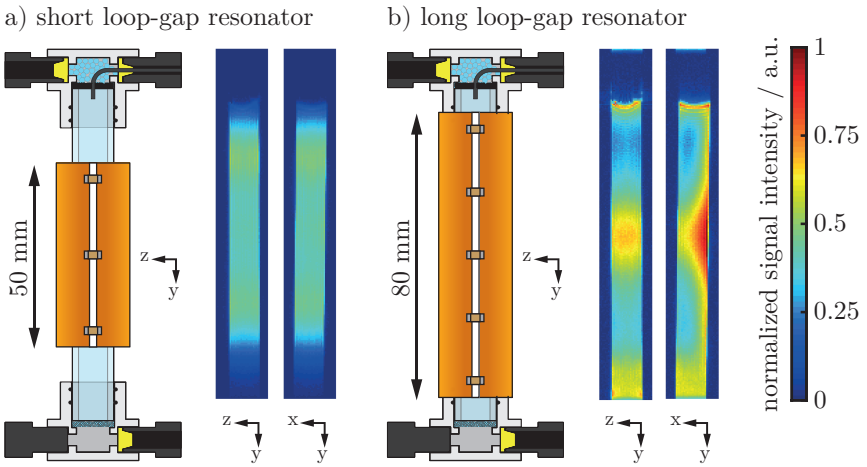

Fig. 8.7 Signal intensities of a deionized water sample inside two cross sections (Y-X, Y-Z). Two loop-gap resonators of different length were tested. The short 50 mm resonator (a) shows a rather constant signal across the whole field of view, whereas the long 80 mm resonator (b) has some strongly pronounced intensity maxima and minima.

8.4 Development of an MRI Method for Taylor Flow Investigations

When performing an MR experiment, the specific method can be chosen from a large variety of different pulse sequences to obtain the data of interest. The measured data result as a response to an applied RF excitation pulse. The data are obtained in the time-domain, describing the system's response to the equilibrium state. Subsequently, a Fourier transformation is used to transform the data into the frequency-domain, providing the MRI image.

8.4.1 Influence of Different MRI Parameters on the Acquired Data

In order to study the influence of different MRI parameters on the resulting images, a series of measurements of an acetonitrile / N_2 system was performed inside the first version of the flow setup with a $d_i = 5$ mm capillary. Acetonitrile was chosen as the liquid phase, as the usage of a contrast agent for MRI investigations of chemical gas-liquid reactions was intended in further steps which relies on acetonitrile as a solvent. A first examination of different flip angles revealed a relationship between greater flip angles and higher signal intensities. Measurements of the fluid at rest showed a partial saturation, resulting in a signal decrease in subsequently acquired images until a steady state was reached after around five to seven images. This effect occurs due to short repetition times of 1000 ms as the system needs sufficiently long to restore its initial magnetization. As soon as liquid flows through

the capillary, the effect gets less visible due to the freshly entering fluid which has not been excited by the MRI sequence before. The saturation effect can only be seen between the first two images.

Further measurements of N_2 bubbles held in a countercurrent flow indicated an increased signal in the vicinity of the bubble. The effect can be seen in Fig. 8.8a. Preparation pulses were used to systematically saturate and suppress the signal arising from the liquid phase, showing only the flow related changes. The effect of pulse preparation is clearly visible in Fig. 8.8b.

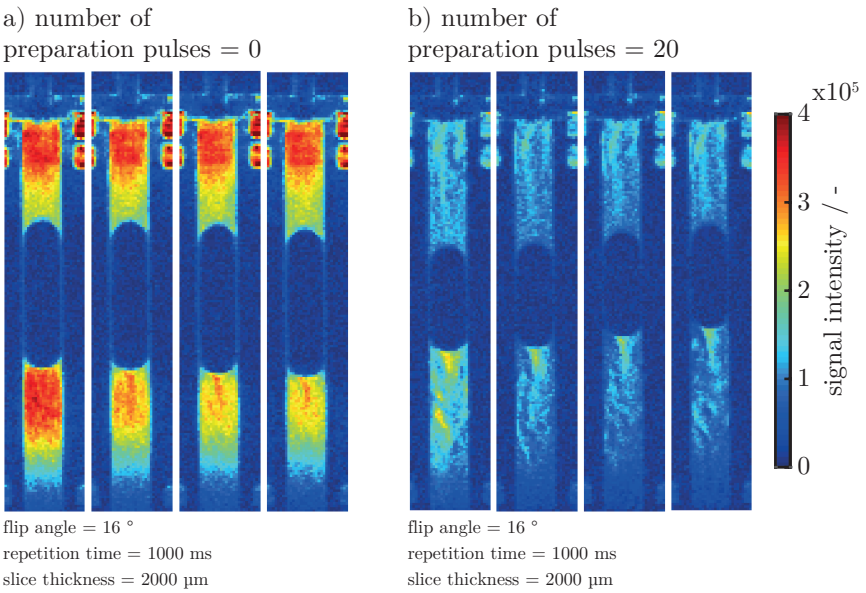

Fig. 8.8 MRI series showing the influence of preparation pulses on the observed wake structure. The flow pattern inside the bubble's wake is visible in both cases. The flow related effect of the liquid phase can be separated by presaturation of the observed slice (b).

In order to understand the investigated flow effect, the thickness of the measurement slice was varied. Fig. 8.9a shows a series of images acquired within a slice of 2 mm thickness. Again, a defined and constant region of increased intensity is located behind the bubble, followed by altering patterns downstream the capillary. The patterns in front of the bubble are mainly caused by swirling motions of the fluid due to high flow velocities at the inlet of the glass capillary.

The observed effect is explained by protons which entered the measurement plane. Initially, the signal of all protons inside the measurement plane was nulled by preparation pulses. Protons which were carried into the measurement plane by the local flow dominated the signal. This particularly happened directly behind the bubble. The effect of an increased measurement slice thickness of 9 mm can be

observed in Fig. 8.9b. As the slice thickness is increased, the signal inside the wake region vanishes. By choosing a slice thickness greater than the capillary's diameter, the flow effect can no longer be mapped.

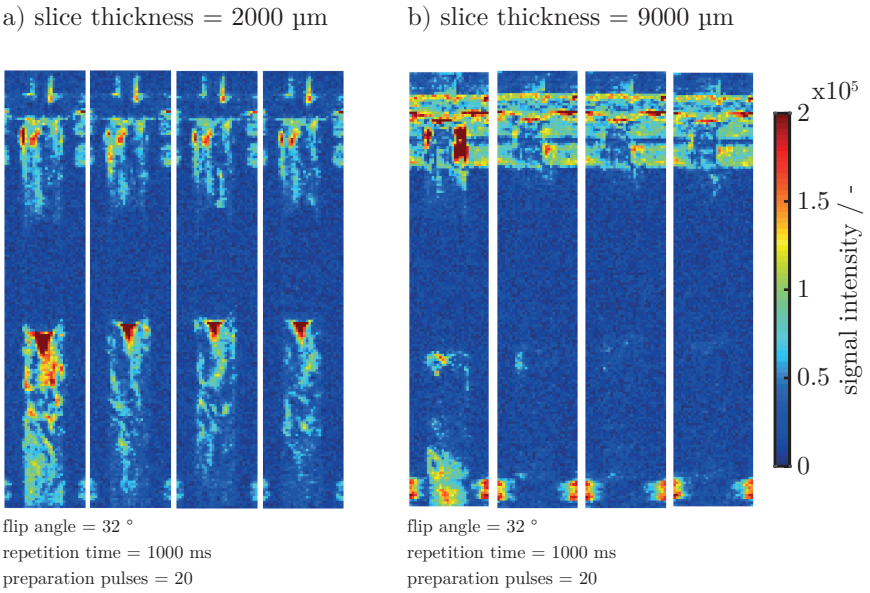

Fig. 8.9 MRI series showing the influence of the measurement slice thickness on the observed wake structure. A slice thickness smaller than the capillary diameter d_i (a) clearly shows structures within the bubble's wake, whereas no structures are visible if a slice thickness greater than d_i is chosen.

8.4.2 Influence of Gas-Liquid Mass Transfer on the Acquired Data

It was additionally checked if mass transfer from the gas phase to the liquid phase has any influence on the measured MRI data. Therefore, the acetonitrile was saturated with N_2. By using pure N_2 as the gas phase, no mass transfer takes place, as shown in Fig. 8.10a. In contrast, mass transfer is enabled by changing the gas phase to O_2. The corresponding results are shown in Fig. 8.10b. Both cases show similar results. Thus, no significant effect of gas-liquid mass transfer on the acquired MRI data was found.

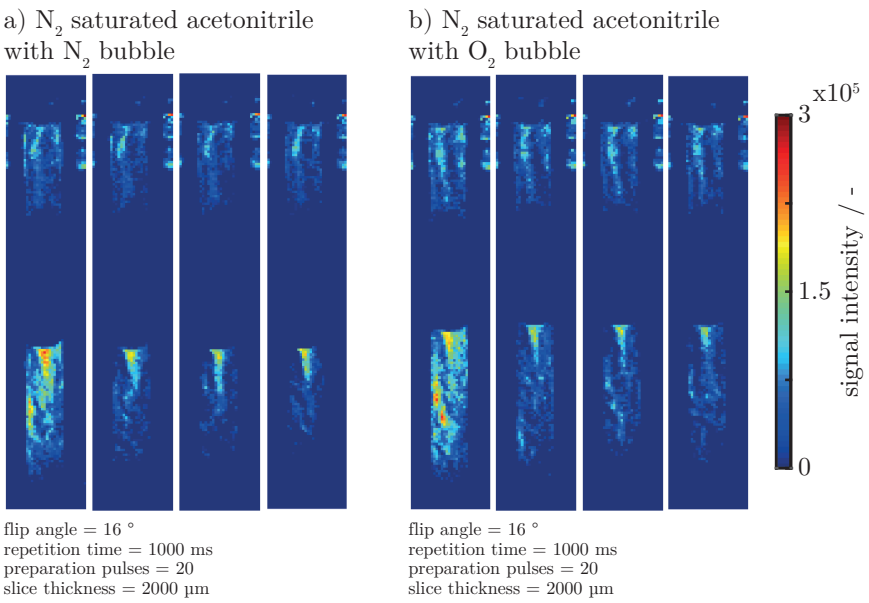

Fig. 8.10 MRI series showing the influence of mass transfer on the observed wake structure. In both cases, without (a) and with (b) mass transfer, the same structure inside the bubble's wake is visible.

Further measurements were carried out using a deionized water / N_2 system inside the improved version of the flow setup with a $d_i = 6$ mm and $d_i = 7$ mm capillary. An exemplary result is given in Fig. 8.11. Even without preparation pulses, no significant flow distortions are visible in front of the bubble.

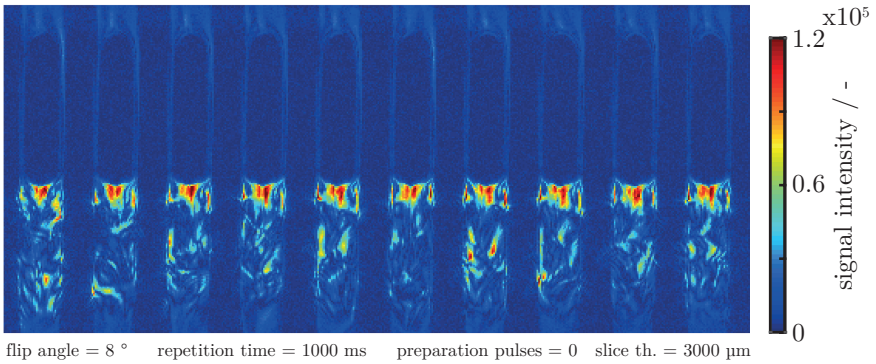

Fig. 8.11 MRI series showing the wake region behind a N_2 bubble inside a deionized water countercurrent flow. A capillary of $d_i = 7$ mm was used. The signal inside the wake is significantly increased.

The results from the water / N_2 experiments were used to develop an MRI sequence for time resolved flow mapping inside the test section. Furthermore, the MRI and PIV data from the $d_i = 6$ mm capillary were acquired under identical hydrodynamic conditions and can be compared with each other to validate the results measured by MRI.

The final flow experiments with the specially developed MRI sequence were conducted with N_2 as the gas phase. N_2 does not contribute to the ^{1}H NMR signal and is therefore completely invisible within the MRI data. Deionized water acted as the liquid phase. To avoid any mass transfer between both phases, the water was saturated with N_2. Preventing mass transfer helps to maintain a constant bubble size which results in a better flow control. The flowrate was manually adjusted to hold the bubble in place. The investigated Taylor bubbles had a length to diameter (l/d) ratio between 2 and 3. The sequence for MRI flow mapping as well as the data acquisition and processing procedures are described in the following sections.

8.4.3 MRI Sequence for Taylor Flow Investigation

A snapshot-FLASH sequence [36] was used for time-resolved flow mapping. Therefore, data were acquired within a vertical single plane through the capillary's center line. Initially, the signal of all water protons inside the measurement plane was nulled by a presaturation module. After a specified delay time t_d, the signal was read out. Water protons which entered the measurement plane during the specified delay time dominated the signal. Increasing the delay time lead to stronger MRI signals, dominated by inflow of unsaturated water protons. The T1 relaxation of stationary spins contributed only partially to the signal. The MR experiments were performed using ParaVision 5.1. A snapshot-FLASH sequence was used and extended by an additional presaturation module. The slice thickness of the acquired MR images was set to 2 mm. A field of view of 42 mm x 16 mm with an isotropic in-plane resolution of 0.5 mm was chosen. A frame rate of 1 Hz was achieved by acquiring an image in four segments with a partial Fourier acceleration rate of 1.5 and an interval of 250 ms. The data read out was performed in parallel direction to the flow (Y-axis) with an echo time of 0.811 ms, excitation pulses of 3 °, an echo position of 30 % and an image bandwidth of 200 kHz. The presaturation module consisted of three slice-selective 90 ° hyperbolic secant pulses, followed by crusher gradients with a total length of 13.46 ms. The delay times t_d were set to 4.88 ms, 24.88 ms, 54.88 ms and 104.88 ms and mark the time span between the last saturation and the first excitation pulse. MR images were acquired in two orthogonal planes. The orientation of the planes is referenced to the convention of MRI magnets, where the front view describes the Y-X and the side view the Y-Z plane.

8.4.4 MRI Data Acquisition and Processing

MRI images were acquired along the capillary's center line. A bubble was manually introduced and placed within the experimental reference frame. The bubble position was monitored by an optical fiber endoscope. 64 images were captured at a frame rate of 1 Hz. Postprocessing of the MRI data was performed in MATLAB to correct possible bubble movement during the experiment. As multiple images were used to calculate the mean data, a precise alignment of the images, with respect to the bubble's rear cap position, was crucial. The data were imported into MATLAB using ParaVision's specific format. Required information were extracted from the method, 2dseq and reco files. A 2d cross-correlation approach (xcorr2) was used for bubble tracking. The bubble position of the first image acted as reference with a region of interest (ROI) of 23 by 23 voxel around the rear cap position. The vertical movement for the whole dataset was calculated with respect to the reference image, resulting in a mean cap position. Valid images were then selected according to two criteria as shown in Fig. 8.12. Firstly, the tolerated movement around the mean position was constrained by manually set boundaries of $\pm$ 2 voxel to eliminate outliners. Secondly, an image was only recognized as valid, if the previous and next cap positions equaled the one under investigation. This helped to prevent artefacts and blurred images from quickly moving bubbles. The valid images were shifted and used to calculate the averaged MRI image and standard deviation. At least 30 valid images were used for the Taylor flow investigations. Additionally, the signal to noise ratio (SNR) was estimated [37] as a measure of quality. A 12 by 12 voxel region inside the wake (signal) was compared to an equally spaced region inside the bubble (noise).

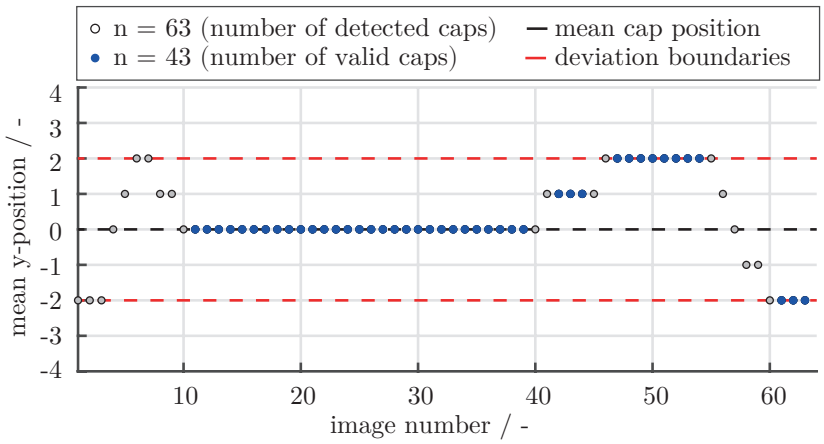

Fig. 8.12 Temporal bubble movement of one exemplarily chosen MRI dataset. The shift around the mean y-position is determined. Valid images (blue dots) are used for further processing.

8.5 MRI of Hydrodynamics Inside Taylor Flows

The hydrodynamics around a N_2 Taylor bubble were investigated by using the improved countercurrent flow setup shown in Fig. 8.2 and the developed MRI specific methods described in 8.4.3. Images were acquired from two cross sections (Y-X, Y-Z) at four different delay times t_d. Water molecules are exchanged between the surrounding volume and the measurement plane during the delay time. Higher flow velocities, as well as longer delay times increase the number of interchanged water molecules, resulting in higher signal intensities. The resulting averaged MRI signal intensities for four different delay times are exemplarily shown for the Y-X plane in Fig. 8.13. Clear distinct flow maxima inside the wake are visible, especially at longer delay times, due to the increased number of exchanged water molecules.

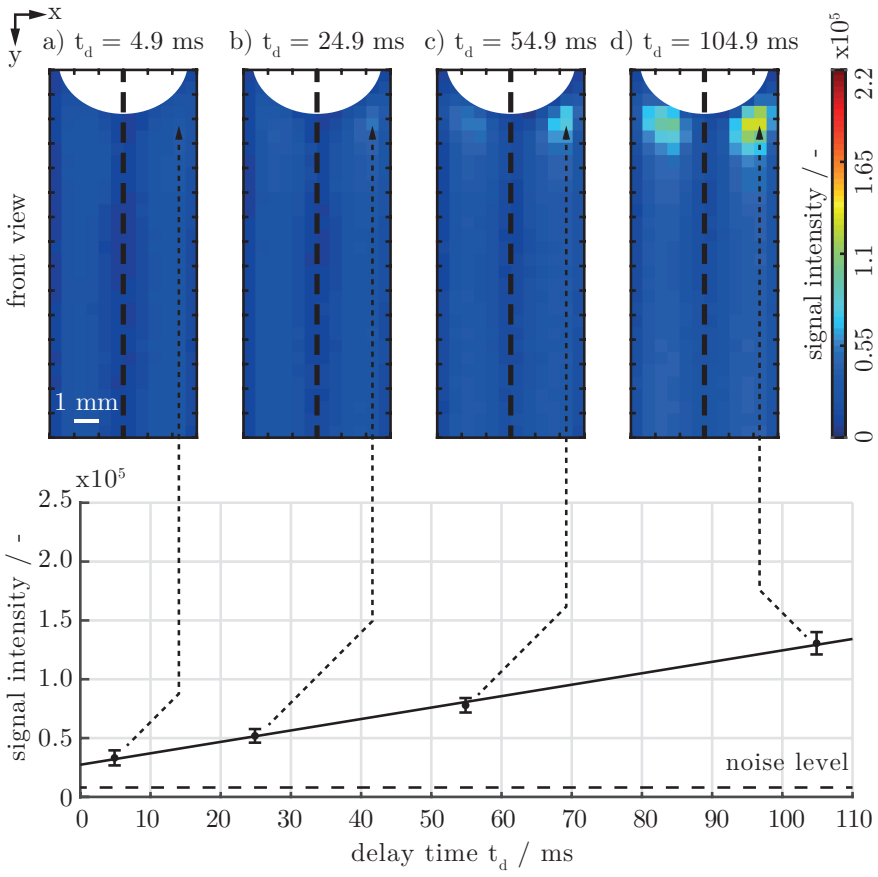

Fig. 8.13 Averaged MRI images of the bubble's wake region inside the Y-X plane. The time-dependent intensity increase of the signal is plotted at the voxel position of the overall highest intensity. The voxel position is additionally indicated by the dashed arrows.

In the Y-X plane, high flow velocities are present on the left and right side of the bubble, whereas the Y-Z plane shows a maximum signal centered below the bubble. The flow pattern shown by the MRI data cannot be characterized as symmetric or homogeneous as the results show neither rotational nor axial symmetry. Previous hydrodynamic investigations of gas-liquid Taylor flows [9, 12] have shown rotational symmetry. Prerequisite for this is a sufficiently long entrance length, allowing the flow to develop. As the experimental MRI setup is limited in height, this requirement cannot be fulfilled. Measures were taken to minimize flow alterations, even at small heights. After the flow enters sideways into the test section, it is deflected downwards by a bed of packed glass beads and passes a small pore glass membrane before entering the capillary. Both, the beads and the membrane, acting as flow straighteners. Additionally, the inertia of the system was kept as low as possible by choosing the smallest possible capillary diameter. With this, alterations of the flow were further reduced but not fully suppressed. However, an advantage can be taken from the present asymmetric and stationary flow field: Systematic errors are eliminated by clearly distinguishing between both cross-sectional views.

In addition to the averaged MRI signals, the time-dependent signal increase is plotted at the voxel position of the overall highest signal intensity and is also exemplarily given in Fig. 8.13. The corresponding voxel positions are indicated by the dashed arrows. Even at short delay times, signal intensities are large enough to differentiate them from background noise, as marked by the dashed horizontal line. This means that fast measurements are possible. However, short delay times will significantly reduce the signal to noise ratio as listed in Table 8.2.

Table 8.2 Number of processed images and SNRs for different delay times of both views

Y-X plane / front view				
Delay time t_d	4.9 ms	24.9 ms	54.9 ms	104.9 ms
Images (n)	44	32	31	33
SNR	3.7	4.4	5.2	6.9
Y-Z plane / side view				
Delay time t_d	4.9 ms	24.9 ms	54.9 ms	104.9 ms
Images (n)	58	33	30	43
SNR	3.4	4.4	5.7	8.2

Even delay times of 104.9 ms were sufficiently short to resolve the present flow field with a high SNR of around 8.2. A signal readout time of around 58 ms would be necessary for a snapshot-FLASH sequence with 32 phase encoding steps. This readout time was significantly reduced by using a partial Fourier acceleration rate of 1.5 to asymmetrically truncate the k-space. The image acquisition was segmented

into four parts with a readout time of 8.9 ms for each segment. This means that all MRI images are marginally biased by flow related artifacts, which are particularly noticeable at short delay times up to several ms with a vanishing impact at long delay times.

Local MRI intensity plots inside the Y-X plane are shown in Fig. 8.14. The distance from the bubble is increased voxel-vise from I to VII, starting directly behind the maximum value. A linear regression line has been fitted, representing the time dependent signal intensity of a given voxel at different delay times. The intensity will presumably reach an overall maximum if sufficiently long delay times are chosen, as all water molecules inside the measurement plane are replaced and longitudinal magnetization is restored by T1 relaxation. At increasing distances from the bubble, a flattening of the slope is observed. This is explained by the stronger radial flow in the vicinity of the bubble, as more water molecules are carried into the measurement plane. This makes the slope an indicator for the amount of flow entering over a given time period, which relates to a measure of velocity. The linearity of the intensity demonstrates the presence of a simple flow inside the wake region without vortices or back mixing.

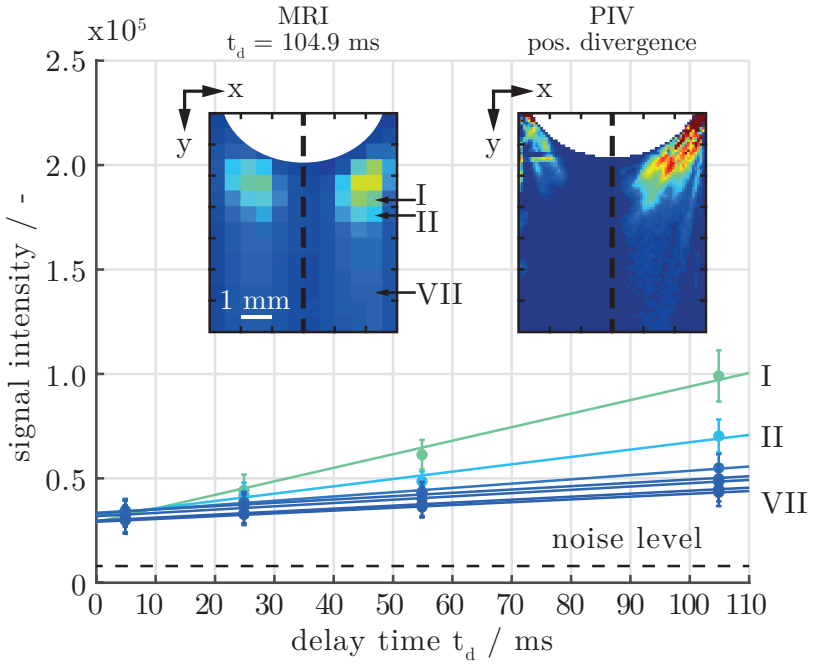

Fig. 8.14 Local MRI intensity plot inside the Y-X plane. The distance from the bubble is increased voxel-vise from I to VII and plotted for all delay times. Additionally, MRI data at t_d=104.9 ms is compared with the divergence calculated from the PIV results. Only the positive part of the divergence is mapped, resembling the same data as obtained from MRI measurements.

To directly compare MRI and PIV results, the divergence of the PIV flow field was calculated. It resembles the flux into (positive part) and out of (negative part) the measurement plane. As the MRI data solely represents the flux into the measurement plane, only the positive part of the divergence was examined. Due to the high spatial resolution and accuracy of the results, PIV is particularly suitable as a reference method for hydrodynamic investigations. Fig. 8.14 exemplarily shows a side-by-side comparison of the measured MRI data and the divergence, calculated from the PIV flow data inside the Y-X plane. The data is normalized for each method between zero and the maximum value inside the wake of the Y-Z plane (not shown here). The stationary, and asymmetrical behavior of the flow field is equally observed in both methods. The Y-X plane reveals two regions of increased flux, located in the vicinity of the bubble with a stronger pronounced signal on the right hand. In contrast, a region of strong flux appears directly centered behind the bubble within the Y-Z plane.

It is important to note that the measurement plane thickness differs between both methods. For the MRI measurements, it is defined by the gradient strength of the experiment and amounts to 2.0 mm. The thickness of 0.725 mm for the PIV measurements is defined by the optical setup's depth of field. Furthermore, it is to mention that MRI measurements were conducted using N_2 whereas PIV measurements used air as the gas phase. The liquid phase was saturated with the used gas phase in all experiments to avoid bubble shrinkage and mass transfer. An influence of the used gas phase on the results can be ruled out, as only hydrodynamic studies without any mass transfer were conducted and N_2 and air have similar physical properties. The MRI experiments benefit from the use of N_2, as it gives no ^{1}H NMR signal. The results show good qualitative agreements between MRI and PIV.

8.6 MRI of Chemical Reactions Inside Taylor Flows

As a first approach to investigate chemical reactions by MRI under real Taylor flow conditions, T1 relaxation time measurements were performed inside the MRI setup. The test section inside the loop-gap resonator was replaced by 2 ml crimp top vials, containing the chemical samples. A Cu(btmgp)I complex was dissolved inside pure acetonitrile and filled into the vials under exclusion of air. At room temperature Cu(btmgp)I experiences a transition of Cu(I) over Cu(III) to Cu(II) which takes place in around 4 s when exposed to dioxygen. The formation of Cu(III) takes places very fast and is assumed to be limited by mass transfer, which means that the decay of the Cu(III) complex is the rate-indicating step of the chemical reaction [38]. The same copper complex was already used for MRI investigations of chemical gas-liquid reactions inside a high-viscous acetonitrile/polyethylene glycol solution ($\eta = 800\,\mathrm{mPa\,s}$) with O_2 bubble rise velocities ranging from $0.14\,\mathrm{mm\,s^{-1}}$ to $0.5\,\mathrm{mm\,s^{-1}}$ [29].

T1 relaxation times of two different Cu(btmgp)I concentrations (1 mmol l^{-1} and 10 mmol l^{-1}) were determined by inversion recovery measurements after the reaction with O_2 (Fig. 8.15).

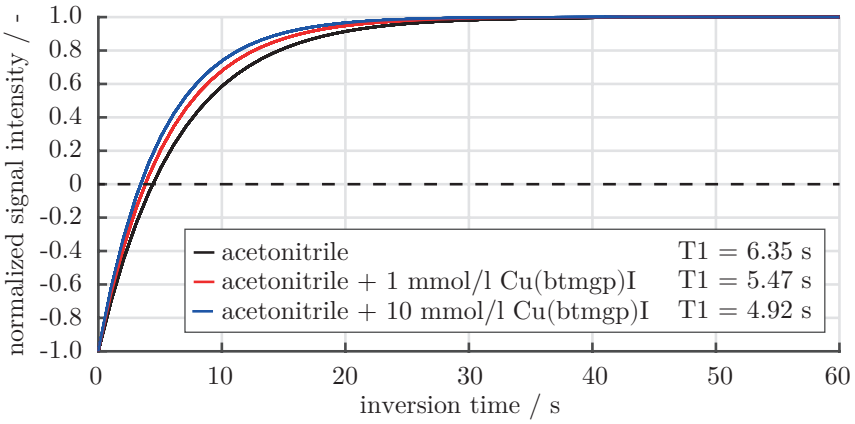

Fig. 8.15 Inversion recovery measurements for T1 relaxation time calculations of pure acetonitrile and two different Cu(btmgp)I concentrations dissolved in acetonitrile.

Compared to pure acetonitrile, a noticeable decrease of the T1 relaxation times with increasing Cu(btmgp)I concentrations after reaction with dioxygen is observed. After contact with dioxygen, T1 and T2 relaxation times are shortened due to the paramagnetic behavior of the formed Cu(II) species [29].

Two fundamental problems are encountered for the investigation of chemical reactions by MRI under real Taylor flow conditions: Firstly, the necessary transition time from Cu(I) to the paramagnetic Cu(II) species lies within in the same order of magnitude as the residence time of the fluid inside the test section. One possible workaround would be to preheat the solution to increase the rate constant of the Cu(III) decay and therefore the formation of Cu(II). A temperature increase of 10 K has shown to cut the decay period by one half [38]. In this case a temperature increase of $\Delta T = 60$ K is required to perform in under 100 ms. This would result in a total temperature just below the boiling point of the solvent. A drawback is the adverse effect of increased temperatures on the SNR of the MRI data. Furthermore, a precise temperature measurement inside the test section is necessary to precisely determine the rate constant of the reaction.

Secondly, the results of Fig. 8.15 show that at short measurement times, as required for fast flow mapping, the signal intensity between the pure solvent and the paramagnetic Cu(II) species is indistinguishable. Choosing higher Cu(btmgp)I concentrations is not an option, as the concentration of 10 mmol l^{-1} already showed a

precipitation inside the sample, which will most likely influence the MRI measurements.

A second chemical reaction system used during this priority programme is the FeII(edta)/NO system[39]. Its color changing reaction has already been used for optical mass transfer studies [2, 20]. The system is currently prepared for MRI Taylor flow investigation at the time of writing. No statement can be made at this point whether the system is suitable for chemical reaction measurements under real Taylor flow conditions or not.

There are many fundamental requirements to successfully perform MRI studies, especially when dealing with fast spatially resolved measurements of chemical reactions inside two-phase flows. Special demands are placed on the experimental setup. It has to fulfill the requirements of MRI compatibility in terms of size, materials, periphery, etc. Ferromagnetic materials cannot be used inside or near the MRI system. The same applies to electrical peripheries such as pumps, cameras, sensors etc. If possible, the usage of any kind of metal should be avoided inside the MRI scanner to prevent eddy currents, resulting in erroneous measurements. Furthermore, a suitable and MRI active reaction system is needed. The kinetics of the reaction need to go well with the residence times inside the investigated setup. Fast kinetics are needed for time-critical investigations of e.g. complex flows. Also, an appropriate MRI sequence for the phenomena or parameters of interest is required. If possible, an existing sequence should be used and potentially modified for the investigated problem. Depending on the investigated flow, a tradeoff between acquisition speed and image quality has to be accepted. If steady state measurements are possible, the image quality can be increased at the cost of losing temporal information by averaging a large number of single images. If complex flows are analyzed, the image resolution has to be adjusted to the required temporal resolution.

8.7 Conclusion and Outlook

Non-invasive flow measurements of pure low-viscous gas-liquid Taylor flows inside a horizontal bore MRI scanner were successfully conducted. For that, a MRI compatible Taylor flow setup and a suitable loop-gap resonator were built. A countercurrent flow configuration was used to conduct measurements over an extended period of several minutes. Preliminary experiments were conducted to develop a suitable MRI sequence for the visualization of Taylor flows.

MRI flow visualization was performed with a modified snapshot-FLASH pulse sequence with presaturation. The sequence was improved in terms of reduced motion blurring and shorter acquisition times. PIV experiments were conducted inside the same flow setup and compared to the MRI results. Taylor flows could successfully be generated inside the setup of limited height, showing an asymmetrical but stationary flow. These asymmetrical flow conditions were beneficial, as they contributed to a better understanding of the developed method. A time dependent flow

analysis is enabled by the introduced variable delay time t_d, allowing to spatially resolve the flow progression over time. A qualitative comparison of both methods reveals certain similarities of local changes in flow, which are in good qualitative agreement.

First tests were performed using a chemical reaction system. The utilized Cu(btmgp)I complex dissolved in the aqueous solution acts as a contrast agent by reducing T1 relaxation times after contact with O_2 entering the solution from the bubble. It could be shown that the reaction kinetics are to slow for the investigated problem. A significant reduction of T1 relaxation times was measured between pure solvent and two concentrations of the copper complex. However, the signal intensities were only marginally different and undistinguishable at low measurement times. Future investigations will be performed for the FeII(edta)/NO reaction system [39].

An initial step in paving the way towards a spatially resolved 3D flow analysis of gas-liquid Taylor flows under relevant flow conditions is presented. The described method for flow analysis provides an important contribution to separately quantify the effect of superimposed chemical reactions. However, the investigation of chemical reactions by MRI under relevant Taylor flow conditions is still at the beginning an especially challenging for low viscous liquids. Future investigations require reaction systems with suitable reaction kinetics as well as fast and distinguishable MRI detectability of reactants and products.

Acknowledgements

The authors gratefully acknowledge funding by the GermanResearch Foundation (DFG) within the priority program SPP 1740 "Reactive Bubbly Flows" (grant TH 893/17-2).

We would like to thank all research groups of the priority programme for the fruitful collaboration and discussions on reactive bubbly flows.

We would like to thank Dipl.-Ing. Ulrich Mießner and Dr. Thorben Helmers for the intensive collaboration during the whole project and the assistance with the PIV experiments.

We would like to thank Melanie Paul and Larissa Laurini from the RWTH Aachen for providing and helping with the Cu(btmgp)I complex used for chemical reactions.

Reference

1. Shen, G., & Finch, J. A. (1996). Bubble swarm velocity in a column. Chemical engineering science, 51(14), 3665-3674.
2. Merker, D., Böhm, L., Oßberger, M., Klüfers, P., & Kraume, M. (2017). Mass transfer in reactive bubbly flows–a single-bubble study. *Chemical Engineering & Technology*, *40*(8), 1391-1399.
3. Kück, U. D., Mießner, U., Aydin, M., & Thöming, J. (2018). Mixing time and mass transfer of rising bubbles in swarm turbulence. Chemical Engineering Science, 187, 367-376.
4. Direito, F. J. N., Campos, J. B. L. M., & Miranda, J. M. (2017). A Taylor drop rising in a liquid co-current flow. International Journal of Multiphase Flow, 96, 134-143.
5. Hayashi, K., Kurimoto, R., & Tomiyama, A. (2011). Terminal velocity of a Taylor drop in a vertical pipe. International Journal of Multiphase Flow, 37(3), 241-251.
6. Helmers, T., Kemper, P., Thöming, J., & Mießner, U. (2019). Modeling the excess velocity of low-viscous Taylor droplets in square microchannels. Fluids, 4(3), 162.
7. Meyer, C., Hoffmann, M., & Schlüter, M. (2014). Micro-PIV analysis of gas–liquid Taylor flow in a vertical oriented square shaped fluidic channel. *International journal of multiphase flow*, *67*, 140-148.
8. Nogueira, S., Riethmuller, M. L., Campos, J. B. L. M., & Pinto, A. M. F. R. (2006). Flow patterns in the wake of a Taylor bubble rising through vertical columns of stagnant and flowing Newtonian liquids: An experimental study. *Chemical engineering science*, *61*(22), 7199-7212.
9. Boden, S., Haghnegahdar, M., & Hampel, U. (2017). Measurement of Taylor bubble shape in square channel by microfocus X-ray computed tomography for investigation of mass transfer. Flow Measurement and Instrumentation, 53, 49-55.
10. Butler, C., Cid, E., & Billet, A. M. (2016). Modelling of mass transfer in Taylor flow: investigation with the PLIF-I technique. Chemical Engineering Research and Design, 115, 292-302.
11. Kastens, S., Hosoda, S., Schlüter, M., & Tomiyama, A. (2015). Mass transfer from single Taylor bubbles in minichannels. Chemical Engineering & Technology, 38(11), 1925-1932.
12. Kastens, S., Timmermann, J., Strassl, F., Rampmaier, R. F., Hoffmann, A., Herres-Pawlis, S., & Schlüter, M. (2017). Test system for the investigation of reactive Taylor bubbles. Chemical Engineering & Technology, 40(8), 1494-1501.
13. Bergman, T. L., Lavine, A. S., Incropera, F. P., & DeWitt, D. P. (2018). Fundamentals of Heat and Mass Transfer (8th ed.). Wiley.
14. White, E. T., & Beardmore, R. H. (1962). The velocity of rise of single cylindrical air bubbles through liquids contained in vertical tubes. *Chemical Engineering Science*, *17*(5), 351-361.
15. Liao, Q., & Zhao, T. S. (2003). Modeling of Taylor bubble rising in a vertical mini noncircular channel filled with a stagnant liquid. *International Journal of Multiphase Flow*, *29*(3), 411-434.
16. Bothe, D., & Reusken, A. (2017). Transport Processes at Fluidic Interfaces. Springer Publishing.
17. Raffel, M., Willert, C. E., Scarano, F., Kähler, C. J., Wereley, S. T., & Kompenhans, J. (2018). Particle Image Velocimetry: A Practical Guide (Experimental Fluid Mechanics) (3rd ed. 2018 ed.). Springer.
18. Felis, F., Strassl, F., Laurini, L., Dietrich, N., Billet, A. M., Roig, V., ... & Loubière, K. (2019). Using a bio-inspired copper complex to investigate reactive mass transfer around an oxygen bubble rising freely in a thin-gap cell. Chemical Engineering Science, 207, 1256-1269.
19. Herres, S., Heuwing, A. J., Flörke, U., Schneider, J., & Henkel, G. (2005). Hydroxylation of a methyl group: synthesis of [Cu2 (btmmO) 2I]+ and of [Cu2 (btmmO) 2] 2+ containing the novel ligand {bis (trimethylmethoxy) guanidino} propane (btmmO) by copper-assisted oxygen activation. Inorganica chimica acta, 358(4), 1089-1095.
20. Hlawitschka, M. W., Oßberger, M., Backes, C., Klüfers, P., & Bart, H. J. (2017). Reactive Mass Transfer of Single NO Bubbles and Bubble Bouncing in Aqueous Ferric Solutions–A

Feasibility Study. Oil & Gas Science and Technology–Revue d'IFP Energies nouvelles, 72(2), 11.
21. Reiser, M. F., Semmler, W., & Hricak, H. (2007). Magnetic Resonance Tomography. Springer Publishing.
22. Stapf, S., & Han, S. (2006). *NMR Imaging in Chemical Engineering* (1st ed.). Wiley-VCH.
23. Britton, M. M. (2017). MRI of chemical reactions and processes. Progress in Nuclear Magnetic Resonance Spectroscopy, 101, 51-70.
24. Sadeghi, M., Mirdrikvand, M., Pesch, G. R., Dreher, W., & Thöming, J. (2020). Full-field analysis of gas flow within open-cell foams: comparison of micro-computed tomography-based CFD simulations with experimental magnetic resonance flow mapping data. *Experiments in Fluids*, *61*, 1-16.
25. Ulpts, J., Kiewidt, L., Dreher, W., & Thöming, J. (2018). 3D characterization of gas phase reactors with regularly and irregularly structured monolithic catalysts by NMR imaging and modeling. *Catalysis today*, *310*, 176-186.
26. Gladden, L. F., & Sederman, A. J. (2017). Magnetic resonance imaging and velocity mapping in chemical engineering applications. Annual review of chemical and biomolecular engineering, 8, 227-247.
27. Hosotani, K., Ono, A., Takeuchi, K., Hashiguchi, Y., & Nagahata, T. (2017). Flow visualization of simple pipe and channel flows obtained by MRI time-slip method. Journal of Visualization, 20(2), 321-335.
28. Tayler, A. B., Holland, D. J., Sederman, A. J., & Gladden, L. F. (2012). Applications of ultrafast MRI to high voidage bubbly flow: measurement of bubble size distributions, interfacial area and hydrodynamics. *Chemical engineering science*, *71*, 468-483.
29. Benders, S., Strassl, F., Fenger, B., Blümich, B., Herres-Pawlis, S., & Küppers, M. (2018). Imaging of copper oxygenation reactions in a bubble flow. *Magnetic Resonance in Chemistry*, *56*(9), 826-830.
30. Stephan, P., Kabelac, S., Kind, M., Mewes, D., Schaber, K., & Wetzel, T. (2019). VDI-Wärmeatlas: Fachlicher Träger VDI-Gesellschaft Verfahrenstechnik und Chemieingenieurwesen (Springer Reference Technik) (German Edition) (12. Aufl. 2019 ed.). Springer Berlin Heidelberg.
31. Rowlands, A. (2017). *Physics of Digital Photography*. IOP Publishing.
32. Helmers, T., Kemper, P., Mießner, U., & Thöming, J. (2020). Refractive index matching (RIM) using double-binary liquid–liquid mixtures. Experiments in Fluids, 61(2), 64.
33. Thielicke, W., & Stamhuis, E. (2014). PIVlab–towards user-friendly, affordable and accurate digital particle image velocimetry in MATLAB. *Journal of open research software*, *2*(1).
34. Mispelter, J., Lupu, M., & Briguet, A. (2015). NMR Probeheads for Biophysical and Biomedical Experiments: Theoretical Principles and Practical Guidelines (2nd Edition) (2nd Revised ed.). Imperial College Press.
35. Mispelter, J., & Lupu, M. (2008). Homogeneous resonators for magnetic resonance: A review. *Comptes Rendus Chimie*, *11*(4-5), 340-355.
36. Haase, A. (1990). Snapshot FLASH MRI. Applications to T1, T2, and chemical-shift imaging. Magnetic Resonance in Medicine, 13(1), 77-89.
37. Dietrich, O., Raya, J. G., Reeder, S. B., Reiser, M. F., & Schoenberg, S. O. (2007). Measurement of signal-to-noise ratios in MR images: influence of multichannel coils, parallel imaging, and reconstruction filters. Journal of Magnetic Resonance Imaging: An Official Journal of the International Society for Magnetic Resonance in Medicine, 26(2), 375-385.
38. Schurr, D., Strassl, F., Liebhäuser, P., Rinke, G., Dittmeyer, R., & Herres-Pawlis, S. (2016). Decay kinetics of sensitive bioinorganic species in a SuperFocus mixer at ambient conditions. *Reaction Chemistry & Engineering*, *1*(5), 485-493.
39. Schneppensieper, T., Wanat, A., Stochel, G., Goldstein, S., Meyerstein, D., & van Eldik, R. (2001). Ligand effects on the kinetics of the reversible binding of NO to selected aminocarboxylato complexes of iron (II) in aqueous solution. *European Journal of Inorganic Chemistry*, *2001*(9), 2317-2325.